**RESEARCH ARTICLE**

Rising Stars

ADVANCED MATERIALS
www.advmat.de

# Phonon Driven Ferroelectricity and Raman Active Modes in Hybrid Organic-Inorganic Perovskites

*Chuanzhao Li, Shurong Yuan, Yixin Li, Zhenyue Wu, Yuanyuan Jin, Kian Ping Loh, and Kai Leng**

**Hybrid organic-inorganic perovskites (HOIPs) have emerged as promising ferroelectric semiconductors, yet the phonon signatures governing their ferroelectricity remain poorly understood. Here, by analyzing the temperature-dependent Raman peak profiles of highly ordered ferroelectric domains in HOIPs, a framework to systematically investigate the dimensionality ($n$)-dependent phonons that are critical to ferroelectric behaviour is established. By tracking phonon evolution across the ferroelectric-to-paraelectric phase transition in HOIPs with different $n$, characteristic modes associated with the ferroelectric symmetry-breaking process are identified. Notably, in the ferroelectric phase of $(BA)_2(MA)_2Pb_3Br_{10}$ ($n = 3$), these modes exhibit a redshift compared to those in $(BA)_2(MA)Pb_2Br_7$ ($n = 2$), reflecting a reduced energy barrier for ferroelectric switching. Density functional theory (DFT) calculations further correlate these modes with their spectral signatures in Raman spectroscopy, particularly highlighting zone-boundary modes that diminish upon transitioning to the paraelectric phase. Polarized Raman mapping further reveals adjacent ferroelectric domains with orthogonal polarization orientations, directly linking phonon activity to domain configuration. This work elucidates the role of phonons in HOIP ferroelectricity, offering insights for tailoring domain-related properties in ferroelectric devices.**

## 1. Introduction

Understanding phonons in ferroelectric materials is critical for advancing their applications in sensors, actuators, and electronic devices.[1–3] Ferroelectrics are broadly classified into proper and improper categories based on the origin of spontaneous polarization.[4] Proper ferroelectrics exhibit a direct coupling between spontaneous polarization and a primary structural distortion, primarily driven by zone-center modes.[5] These materials undergo a structural phase transition where inversion symmetry breaking serves as the primary order parameter, leading to a ferroelectric phase. Classic examples include perovskite oxides such as $BaTiO_3$[6] and $PbTiO_3$,[7] where ferroelectricity arises from cooperative ionic displacements within the unit cell. In contrast, improper ferroelectrics develop polarization as a secondary effect, induced by a primary order parameter unrelated to polarization. Here, ferroelectricity emerges from complex couplings between multiple order parameters-such as structural distortions, magnetic ordering, or charge density waves-with polarization acting as a byproduct.[8] Such mechanisms are often observed in multiferroics (e.g., $BiFeO_3$[9] and $Ca_3Mn_2O_7$[10]), where interactions between lattice distortions and electronic or magnetic degrees of freedom drive the polarization.

In improper ferroelectric hybrid organic-inorganic perovskites (HOIPs), the phonons associated with ferroelectric phase transition (referred to as ferroelectric phonons) arise from the anharmonicity of lattice vibrations, involving octahedral tilts and distortions of the inorganic framework that are coupled to the motions of organic cations.[1,11–13] Both the organic and inorganic components collectively influence the ferroelectric transitions in HOIPs, with the organic cations modulating the Curie temperature ($T_c$) and polarization dynamics.[14–16] Understanding the behaviour of these characteristic ferroelectric phonons is important for several reasons. First, they significantly mediate exciton dynamics by introducing additional dephasing channels for excitonic states, which can reduce the coherence times of emitted photons.[17–20] Second, when an electric field is applied to switch polarization, it induces changes in the lattice structure through these characteristic phonons.[21–23] The changing of these phonons is associated with structural phase transitions at elevated temperatures or under external perturbations.[24–27] Variations in the frequency of these phonons provide insights into phase stability and the activation barrier for ferroelectric switching.[23,28,29] To deepen our understanding of the

---

C. Li, S. Yuan, Y. Li, Z. Wu, Y. Jin, K. P. Loh, K. Leng
Department of Applied Physics
The Hong Kong Polytechnic University
Hung Hom, Kowloon, Hong Kong, China
E-mail: kathy-kai.leng@polyu.edu.hk

The ORCID identification number(s) for the author(s) of this article can be found under https://doi.org/10.1002/adma.202419685

**DOI: 10.1002/adma.202419685**

ferroelectric properties of HOIPs and the mechanisms driving phase transitions, it is essential to investigate the behaviour of ferroelectric phonons over a wide temperature range and across varying *n* of HOIPs, particularly those with $n > 1$. By controlling the angle of the linear polarization of the excitation laser relative to the in-plane axes of the inorganic octahedral layer, we can gain detailed information about the symmetry of the vibrational modes and their correlation to the ferroelectric polarization axis. However, a systematic study of these characteristic phonons in relation to HOIP ferroelectrics is currently lacking.

In this work, we identify distinct ferroelectric phonons across different values of *n* in HOIPs using temperature-dependent Raman spectroscopy on ferroelectric domains. Specific vibrational modes become observable in the Raman spectrum when symmetry breaking occurs in the presence of ferroelectric domains and vanish when symmetry is restored, coinciding with the disappearance of ferroelectric domains. This behaviour serves as a hallmark for distinguishing ferroelectric phonons. While it is known that certain Raman-active modes shift with increasing temperature due to lattice expansion or anharmonicity induced by the thermal motion of organic cations,[26,30–32] there is a lack of reports correlating these phonons with ferroelectric-to-paraelectric transitions in HOIPs, as well as their association with different *n* values. By combining our experimental results with DFT calculations, we identify the characteristic ferroelectric phonons and their roles in ferroelectric phase transition. Furthermore, we map ferroelectric domains to identify the phonons associated with the polarization axis. Our findings reveal that HOIPs with higher *n* values exhibit a lower energy barrier for ferroelectric switching, as confirmed by piezoresponse force microscopy (PFM) lithography measurements. This suggests that dimensionality plays a critical role in determining ferroelectric switching behaviour. Our study provides deeper insights into the phonon mechanisms driving ferroelectricity and its loss at elevated temperatures. This understanding may advance knowledge of ferroelectric HOIPs and pave the way for further studies on domain-dependent ferroelectric properties and their applications.

## 2. Results and Discussion

Ferroelectric domains with unique polarization directions serve as valuable tools for visualizing and monitoring the switching of ferroelectric properties.[22,33,34] However, preparing HOIPs with well-aligned ferroelectric domains is challenging. Fortunately, we have discovered that exfoliated $(BA)_2(MA)_{n-1}Pb_nBr_{3n+1}$ ($n > 1$) (where BA is butylamine and MA is methylamine) with specific thicknesses can exhibit highly order ferroelectric domains observable under a polarized optical microscope (POM). While previous studies have focused on bulk, macroscopic ferroelectric properties,[35,36] there has been limited research on the properties of ferroelectric domains in $(BA)_2(MA)_{n-1}Pb_nBr_{3n+1}$. In this work, we analyze the phonons in ferroelectric domains to gain deeper insight into the mechanisms driving ferroelectricity in HOIPs. As $(BA)_2(MA)_{n-1}Pb_nBr_{3n+1}$ (abbreviated as Br-RPP) crystals are archetypical 2D Ruddlesden-Popper hybrid perovskites (RPPs), our findings are expected to have broad applicability.

We observed highly ordered striped domains with widths of tens of micrometers under POM (**Figure** 1a) for this class of materials. Previous work has confirmed the presence of ferroelastic domains in $(BA)_2(MA)_{n-1}Pb_nI_{3n+1}$ ($n > 1$).[37] In this study, we substitute iodine with bromine to investigate the emergence of ferroelectric domains in Br-RPPs with $n > 1$. Differential Scanning Calorimetry (DSC) curves for $n = 1$, 2 and 3 Br-RPP crystals reveal that they undergo reversible phase transitions at ≈383, 352, and 315 K upon heating, respectively (Figure S1, Supporting Information). At room temperature (300 K), $(BA)_2PbBr_4$ ($n = 1$) crystallizes in the nonpolar orthorhombic space group *Pbca* (point group *mmm*), while both $n = 2$ and $n = 3$ Br-RPP crystals adopt the polar orthorhombic space group $Cmc2_1$ (point group *mm*2),[38] which is characteristic of a ferroelectric phase (FEP).[11,35] During the heating process, both $n = 2$ and $n = 3$ Br-RPPs transition to the centrosymmetric *I*4/*mmm* (point group 4/*mmm*), corresponding to the paraelectric phase (PEP). Both $n = 2$ and $n = 3$ Br-RPP crystals undergo reversible ferroelectric phase transitions, with $T_c$ of ≈352 and 315 K, respectively.

To confirm the ferroelectric nature of the observed striped domains in Br-RPPs with $n > 1$, we conducted PFM. Figure 1b illustrates the piezoresponse for the area highlighted in Figure 1a. Our lateral PFM phase image distinctly shows striped ferroelectric domains in $(BA)_2(MA)Pb_2Br_7$ ($n = 2$), where the adjacent bright and dark striped domains demonstrate an ≈180° phase contrast. Additionally, Figure 1c presents a butterfly-shaped amplitude hysteresis loop, indicating switchable ferroelectric polarization for the $n = 2$ Br-RPP. Finally, the phase versus bias voltage curve, a characteristic feature of ferroelectricity, is depicted in Figure 1d.

Next, we utilized ferroelectric domains to visualize the ferroelectric phase transition. As shown in Figure 1e–h and Figure S2 (Supporting Information), when the temperature of the domains is raised above the $T_c$ of 352 K for $n = 2$ Br-RPP, the domains disappear as the crystal undergoes a phase transition from FEP to PEP. Consequently, the striped ferroelectric domains completely vanish at ≈360 K. However, upon cooling the domains to room temperature, the striped domains re-emerge (Figure 1h–j; Figure S2, Supporting Information), demonstrating the robustness of the ferroelectric phase transition process. Second harmonic generation (SHG) is an effective method for identifying polar phases, as it occurs exclusively in non-centrosymmetric materials.[3,11] Consistent with the phase transitions observed in Figure 1e–h, when the laser is scanned along the 1D striped domain during a simultaneous temperature ramp, the SHG intensity gradually decreases as the temperature increases and eventually disappears completely at $T_c$. Remarkably, the SHG intensity reappears when the sample is cooled to room temperature, indicating that SHG can track the inversion symmetry breaking process in ferroelectric Br-RPPs with $n > 1$. We also repeated these measurements for the $n = 3$ Br-RPP (Figure S3, Supporting Information) to verify its ferroelectric phase.

By clarifying the temperature range that induces the phase transition from FEP to PEP, we can distinguish the characteristic phonons that experience changes in both frequency and intensity during this transition. It is generally understood that as thermal activation occurs, anharmonic effects become predominant, causing certain vibrational modes to become less pronounced due to energy transfer with other modes.[39] Additionally, as the temperature increases, the lattice may expand, leading to increased bond lengths and corresponding decrease in phonon frequencies or less pronounced phonons.[40] In this analysis, we

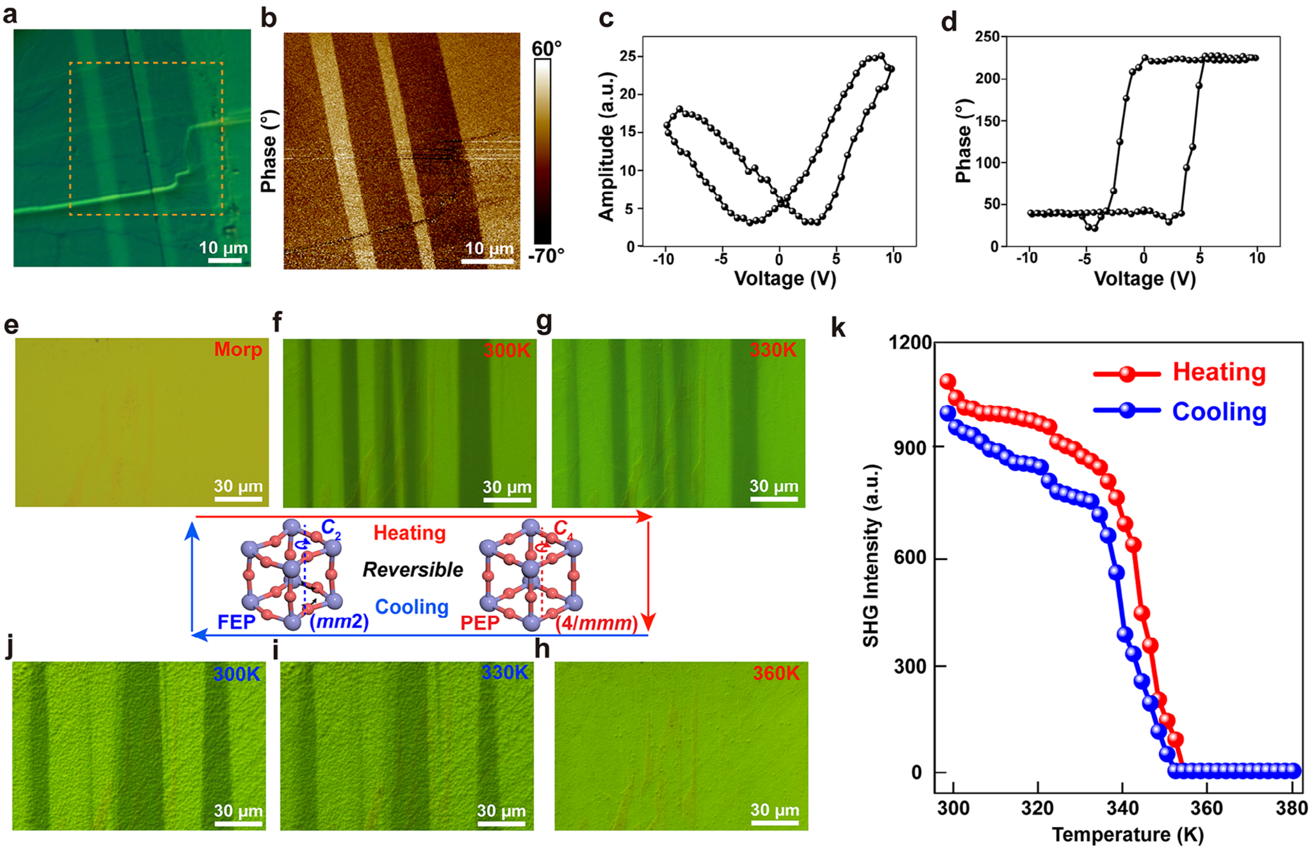

**Figure 1.** Visualization of ferroelectric phase transition in HOIP using ferroelectric domains. a) POM image showing highly ordered striped domains in $(BA)_2(MA)Pb_2Br_7$ ($n = 2$). b) Corresponding lateral PFM phase scan of the area highlighted by the dashed line in a). c) Amplitude versus bias voltage curve for $n = 2$ Br-RPP. d) Phase versus bias voltage curve for $n = 2$ Br-RPP. e–j) Reversible appearance-disappearance of striped ferroelectric domains due to the ferroelectric phase transition during heating and cooling processes. k) Temperature-dependent SHG intensity change during heating and cooling processes.

will not discuss peaks with frequencies below 25 $cm^{-1}$, as these may be mixed with zone-folded longitudinal acoustic phonons corresponding to the periodicity of the entire layered structure.[41] During the heating and cooling processes around the $T_c$ of 350 K for the $n = 2$ Br-RPP single domain, a sharp Raman peak at ≈46 $cm^{-1}$ shows distinct temperature-dependent behaviour, as highlighted in pink in **Figure** 2a,b. As the temperature gradually increases from 300 K to $T_c$ (≈350 K), its intensity decreases, accompanied by a redshift, before vanishing at $T_c$. Upon cooling to room temperature, the peak at ≈46 $cm^{-1}$ re-emerges and gradually shifts back to higher frequencies. The temperature profile of the phonon at ≈46 $cm^{-1}$ is consistent with the reversible ferroelectric-paraelectric transition depicted in Figure 1. Therefore, we suggest the ≈46 $cm^{-1}$ phonon as a characteristic mode indicative of ferroelectricity in $n = 2$ Br-RPP.

Next, we conducted theoretical calculations to simulate the phase transition process from the low-symmetry (LS) phase (ferroelectric, $Cmc2_1$) to the high-symmetry (HS) phase (paraelectric, $I4/mmm$) for $n = 2$ Br-RPP. This analysis aims to examine how changes in point group symmetry during the transition influence the Raman modes.[42,43] The DFT-calculated Raman spectrum for the LS phase of $(BA)_2(MA)Pb_2Br_7$ ($n = 2$) is presented in **Table** 1 (left). This spectrum features Raman-active modes characterized by irreducible representations (irreps) $A_1$, or $B_2$, most of which correspond to coupled organic-inorganic vibrations (Table S1, Supporting Information). Importantly, after the phase transition to the HS phase, certain Raman-active modes become inactive due to the increased symmetry. To identify which Raman-active modes become inactive during the phase transition, we construct a hypothetical HS phase and project the modes from the LS phase onto this newly defined structure. Notably, a mode at the zone-center Γ-point of the LS phase can be projected onto both the zone-center Γ- and zone-boundary $X$-points of the HS phase.[44] The projections of the modes onto the constructed HS phase are summarized in Table 1 (right). If a projected mode is dominated by $A_{1g}$ or $B_{1g}$ (as indicated by the amplitude of the irreps shown in parentheses in Table 1, right), it is likely to remain Raman-active in the HS phase, inherited from the LS phase. Conversely, if the projected mode is dominated by $E_u$ or zone-boundary modes, it becomes Raman-inactive in the HS phase. Combined with our experimental observations of ferroelectric phonons in the range of 40 to 53 $cm^{-1}$ for $n = 2$ (Figure 2b), the theoretical phonons in the range of ≈53 to 61 $cm^{-1}$ (Table 1), which transition from being Raman-active in the LS phase to Raman-inactive in the HS phase, align well with our experimental findings. Since the calculations were performed at 0 K using the harmonic approximation, small

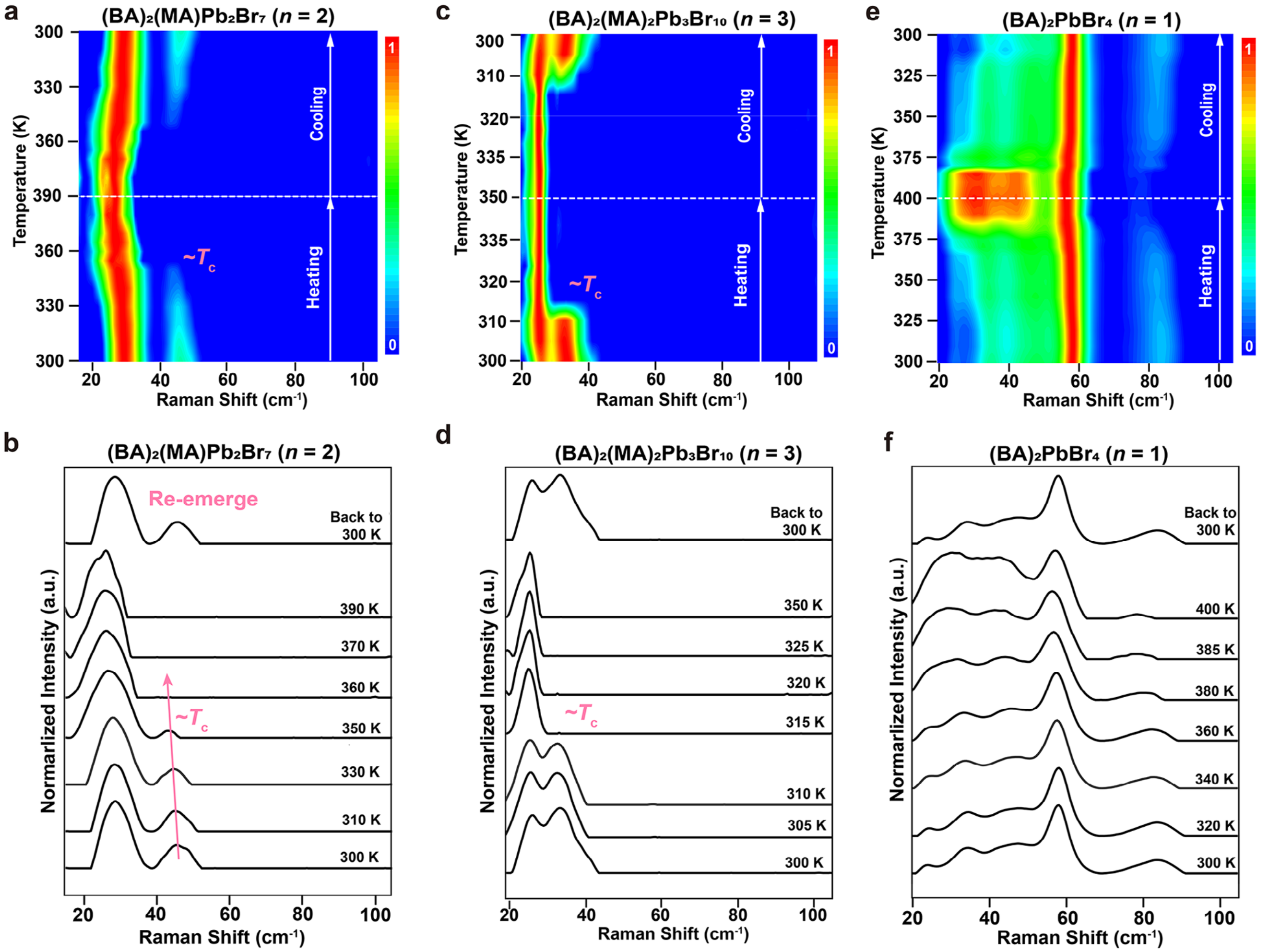

**Figure 2.** Distinguishing the characteristic phonons associated with the ferroelectric phase transition. a,b) Raman mapping and corresponding spectra upon the heating and cooling process from 300 to 390 K and from 390 to 300 K in $n = 2$ Br-RPP. c,d) Raman mapping and corresponding spectra upon the heating and cooling process from 300 to 350 K and from 350 to 300 K in $n = 3$ Br-RPP. e,f) Raman mapping and corresponding spectra upon the heating and cooling process from 300 to 400 K and from 400 to 300 K in $n = 1$ Br-RPP.

**Table 1.** DFT calculations simulate the transition from FEP to PEP of $(BA)_2(MA)Pb_2Br_7$ ($n = 2$) to track the changes in Raman modes from active to in-active.

| Peak | Freq. [cm$^{-1}$] | Irrep | Raman activity in LS phase | Br-Pb-Br description | Projection on the HS phase Zone-center Γ-point | Zone-boundary *X*-point | Raman activity in HS phase |
|---|---|---|---|---|---|---|---|
| C | 25.0 | $B_2$ | Active | scissoring | $B_{1g}$ (0.16) + $E_u$ (0.82) | $X_1^+$ (0.50) + $X_4^-$ (1.21) | In-Active |
| | 25.2 | $A_1$ | Active | rocking | $A_{1g}$ (0.84) + $E_u$ (0.65) | $X_2^+$ (0.24) + $X_3^-$ (1.38) | In-Active |
| D | 29.9 | $A_1$ | Active | wagging + tilting | $A_{1g}$ (0.90) + $E_u$ (2.99) | $X_2^+$ (0.15) + $X_3^-$ (0.69) | In-Active |
| | 30.6 | $B_2$ | Active | twisting + tilting | $B_{1g}$ (0.50) + $E_u$ (1.86) | $X_1^+$ (1.72) + $X_4^-$ (0.72) | In-Active |
| | 32.7 | $B_2$ | Active | twisting + tilting | $B_{1g}$ (0.40) + $E_u$ (1.85) | $X_1^+$ (0.53) + $X_4^-$ (0.72) | In-Active |
| E | 42.4 | $A_1$ | Active | rocking + stretching | $A_{1g}$ (1.33) + $E_u$ (0.98) | $X_2^+$ (0.54) + $X_3^-$ (0.46) | Active |
| F | 53.7 | $A_1$ | Active | rocking | $A_{1g}$ (0.48) + $E_u$ (0.58) | $X_2^+$ (0.57) + $X_3^-$ (0.67) | In-Active |
| | 56.8 | $B_2$ | Active | wagging | $B_{1g}$ (0.05) + $E_u$ (0.94) | $X_1^+$ (0.76) + $X_4^-$ (0.94) | In-Active |
| | 60.8 | $A_1$ | Active | scissoring | $A_{1g}$ (0.66) + $E_u$ (1.88) | $X_2^+$ (0.16) + $X_3^-$ (0.76) | In-Active |
| G | 71.8 | $A_1$ | Active | rocking + wagging | $A_{1g}$ (1.08) + $E_u$ (1.66) | $X_2^+$ (0.51) + $X_3^-$ (1.00) | In-Active |
| | 73.7 | $B_2$ | Active | scissoring + twisting | $B_{1g}$ (0.55) + $E_u$ (0.87) | $X_1^+$ (0.89) + $X_4^-$ (0.90) | In-Active |
| H | 78.8 | $B_2$ | Active | scissoring | $B_{1g}$ (0.06) + $E_u$ (1.44) | $X_1^+$ (0.57) + $X_4^-$ (1.11) | In-Active |
| I | 88.5 | $B_2$ | Active | scissoring + stretching | $B_{1g}$ (0.21) + $E_u$ (2.76) | $X_1^+$ (0.82) + $X_4^-$ (0.67) | In-Active |

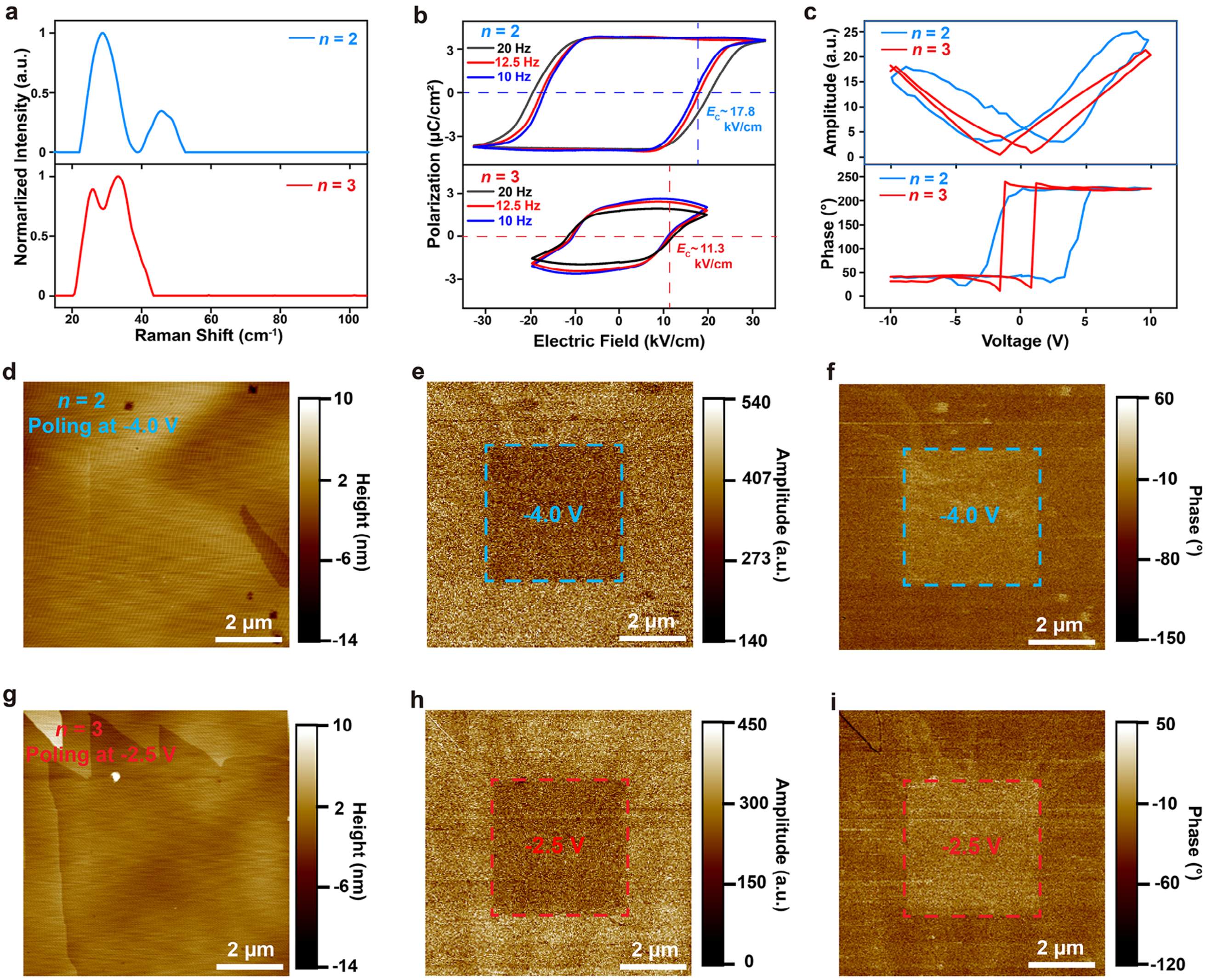

**Figure 3.** Switching PFM verifying a lower energy barrier for ferroelectric switching with a higher $n$ value in Br-RPP film. a) Comparative Raman spectra of $n = 2$ and $n = 3$ Br-RPPs at 300 K. b) $P$-$E$ loops for $n = 2$ and $n = 3$ Br-RPPs at different frequencies. c) Amplitude and phase as a function of bias voltage for $n = 2$ and $n = 3$ Br-RPPs. d–f) Topography image, PFM amplitude image and phase image of an $8 \times 8$ μm² region in $n = 2$ Br-RPP film after applying a tip voltage of −4.0 V. g–i) Topography image, PFM amplitude image and phase image of an $8 \times 8$ μm² region in $n = 3$ Br-RPP film after applying a tip voltage of −2.5 V.

shifts between the calculated and experimental frequencies (measured at ≥300 K) are expected. This agreement further reinforces the conclusion that zone-boundary phonons drive the transition to the ferroelectric phase in our ferroelectric Br-RPP system.

To investigate the $n$-dependence of the ferroelectric phonons, we examine $n = 3$ Br-RPP. A phonon peak at ≈33 $\text{cm}^{-1}$ is observed to vanish at $T_c$ of 315 K and reappear at temperature below $T_c$, which we identify as the characteristic ferroelectric phonons for $n = 3$ Br-RPP (Figure 2c,d). We note that the ≈33 $\text{cm}^{-1}$ Raman peak exhibits a redshift with respect to the ≈46 $\text{cm}^{-1}$ peak observed in $n = 2$ Br-RPP. For $n = 1$ Br-RPP, its Raman spectral profile does not change significantly from 300 to 400 K (Figure 2e,f), which is consistent with the lack of ferroelectric phase transition,[13] as opposed to $n = 2$ and $n = 3$ Br-RPPs. However, Raman peak intensity changes at ≈87, ≈35, and ≈25 $\text{cm}^{-1}$ are observed with increasing temperature, which are associated with non-ferroelectric structural changes. These changes are primarily driven by the disordering of the $\text{BA}^+$ cation and the relaxation of highly anharmonic octahedral tilting,[45] which are not associated with phonons for ferroelectric phase transition. Overall, the spectral profile change with temperature in the case of $n = 1$ Br-RPP is quite different from those of $n = 2$ and $n = 3$ Br-RPPs. This enables us to distinguish the FEP to PEP transition of $n = 2$ Br-RPP and $n = 3$ Br-RPP from the non-ferroelectric $n = 1$ Br-RPP.

The ferroelectric phonon peak in $n = 3$ Br-RPP exhibits a significant redshift compared to those in $n = 2$ Br-RPP in the ferroelectric phase (**Figure 3**a). To investigate whether this redshift influences ferroelectric switching, we performed PFM measurements. Polarization ($P$) versus electric field ($E$) hysteresis loops (Figure 3b) reveal a notable difference in coercive fields: $n = 2$ Br-RPP requires ≈17.8 kV $\text{cm}^{-1}$, substantially higher than the

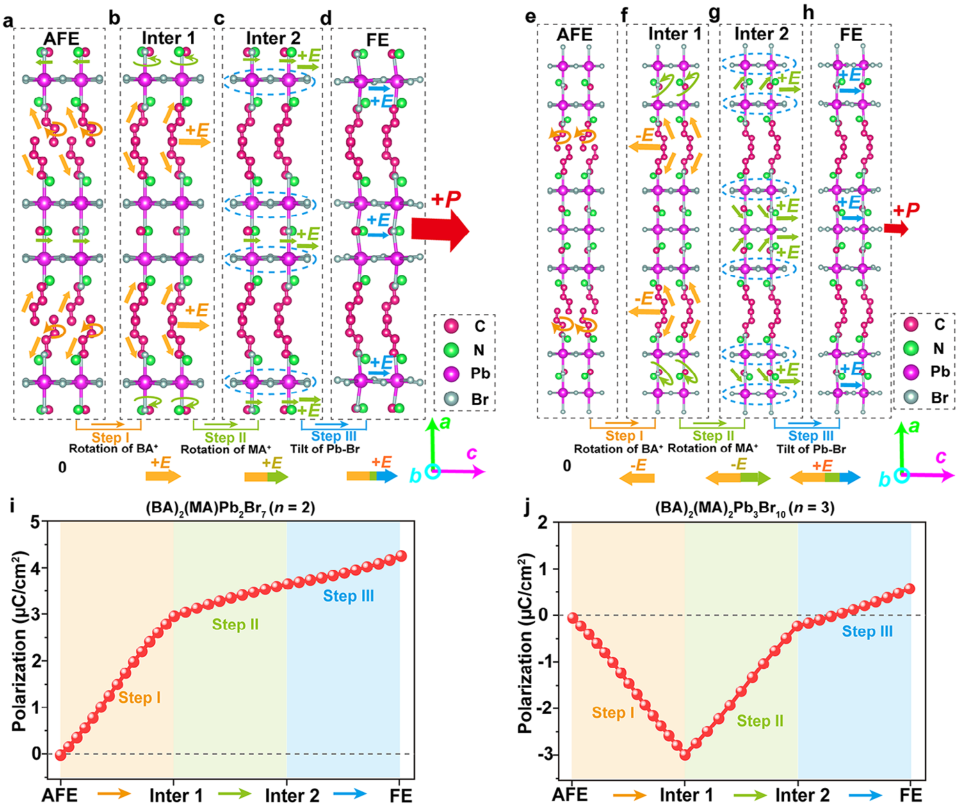

**Figure 4.** Berry phase calculation of spontaneous polarization for $n = 2$ and $n = 3$ Br-RPPs. a–d) Illustration of the dynamic steps from the AFE to the FE phase transition in $(BA)_2(MA)Pb_2Br_7$. e–h) Illustration of the dynamic steps from the AFE to the FE phase transition in $(BA)_2(MA)_2Pb_3Br_{10}$. These steps, which pass through two intermediate phases, primarily involve the rotational motion of the $BA^+$ and $MA^+$ cations around the out-of-plane $a$-axis, as indicated by the yellow and green curved arrows. i,j) The polarization values for each step in $n = 2$ and $n = 3$ Br-RPP based on Berry phase calculations.

≈11.3 kV cm$^{-1}$ for $n = 3$ Br-RPP across multiple scanning frequencies. This trend is corroborated by butterfly-shaped amplitude hysteresis loops and 180° phase reversal curves (Figure 3c), obtained by sweeping the tip voltage from −10 to 10 V. Critically, the inflection point for complete polarization switching in $n = 3$ Br-RPP occurs at lower voltage. For example, during positive voltage scans starting at 0 V, the amplitude loop inflection appears at ≈0.8 V for $n = 3$ Br-RPP versus ≈3.3 V for $n = 2$ Br-RPP. Similarly, phase-voltage curves show that full domain switching in $n = 2$ Br-RPP requires ≈3.1 V, compared to ≈1.2 V for $n = 3$ Br-RPP. These results collectively demonstrate that $n = 3$ Br-RPP undergoes ferroelectric domain switching at reduced electric fields, consistent with its lower coercivity. Additionally, we performed the PFM lithography to directly observe the ease of ferroelectric domain switching in $n > 1$ Br-RPP film. An electrically biased tip with a voltage of −4.0 V was scanned over the central region in $n = 2$ Br-RPP as shown in Figure 3d. The results from switching spectroscopy PFM presented in Figure 3e,f clearly demonstrate that the tip-induced voltage exceeds the local coercive voltage in $n = 2$ Br-RPP, allowing for observable domain reversal in the scanned area. In contrast, the same switching spectroscopy PFM technique applied to $n = 3$ Br-RPP shows that a tip voltage of only −2.5 V is sufficient to induce ferroelectric domain reversal (Figure 3g–i). This contrasting switching behaviour further supports the concept illustrated in Figure 3a, showing that the redshifted ferroelectric phonon peak in $n = 3$ Br-RPP is associated with a lower energy barrier for ferroelectric switching.

To elucidate the lower energy barrier for ferroelectric switching in $n = 3$ Br-RPP compared to $n = 2$ Br-RPP, we performed Berry phase calculations to analyze polarization mechanisms. Hypothetical centrosymmetric antiferroelectric (AFE) phases were modeled for both materials, derived from their respective ferroelectric (FE) phase unit cells. These structures were generated by rotating $BA^+$ and $MA^+$ cations around the $a$-axis and displacing the inorganic Pb-Br framework. Three-step pathways connecting the AFE and FE phases were constructed to simulate polarization evolution (**Figure** 4a–d for $n = 2$; Figure 4e–h for $n = 3$). For $n = 2$ Br-RPP, initial $BA^+$ cation rotation induces polarization along the $+c$ axis (Figure 4b, yellow arrow). Subsequent $MA^+$ cation rotation and Pb-Br framework displacement reinforce this direction (Figure 4c,d, green and blue arrows), yielding a net polarization of 4.22 μC cm$^{-2}$ in the FE phase (Figure 4d, red arrow). In contrast, $n = 3$ Br-RPP exhibits distinct behaviour: $BA^+$ rotation initially polarizes the system along the $-c$ axis (Figure 4f, yellow arrow). However, subsequent $MA^+$ rotation and Pb-Br framework tilting reverse the polarization to $+c$ (Figure 4g,h), counteracting the initial $BA^+$-driven contribution. This antagonistic interplay results in a markedly reduced net polarization of 0.63 μC cm$^2$ (Figure 4h, red arrow), consistent with its lower switching energy barrier.

The polarization values and mechanism in $n = 2$ and $n = 3$ Br-RPPs, based on Berry phase calculations,[46] are depicted in

Figure 4i,j, respectively. To examine the contribution roles of the $MA^+$ and $BA^+$ cations in the polarization of the system in detail, we calculated their dipole moments using a point-charge model, with electron distribution determined by Bader charge analysis.[47] For $n = 2$ Br-RPP in the AFE phase, the dipole moments were calculated to be {±1.36 (along $a$), ±0.64 (along $b$), ±0.58 (along $c$)} e·Å for $BA^+$ cations and {0, ±0.26, ±0.12} e·Å for $MA^+$ cations, respectively. Here, the "+" and "-" signs represent dipole moments of different cations with opposite orientation; while the numbers represent the magnitude of dipole moment. Consequently, the compensation of the dipole moments in all directions results in no net polarization for $n = 2$ in the AFE phase (Figure 4a). During the transition from the AFE to the FE phase, the rotation of the $BA^+$ and $MA^+$ cations around the $a$-axis alters their dipole moments to {±1.32, ±0.61, 0.58} e·Å for $BA^+$ cations and {0, ±0.25, 0.13} e·Å for $MA^+$ cations, respectively. This change leads to net dipole moments along the $+c$ direction in the FE state. In contrast, for $n = 3$ Br-RPP, the rotation of the $BA^+$ and $MA^+$ cations generates dipole moments of {±1.40, ±0.51, −0.58} e·Å and {±0.13, ±0.21, 0.17} e·Å during the AFE to FE phase transition, with the opposite dipole moments along the $-c$ and $+c$ direction, respectively. This results in a significantly smaller polarization value compared to $n = 2$ Br-RPP, which is consistent with our experimental results shown in Figure 3. This analysis also clearly indicates that the net dipole moment contributed by the rotations of the $MA^+$ and $BA^+$ cations have to be considered to determine the overall magnitude of ferroelectric polarization.

To understand the orientation of ferroelectric polarization in relation to the proposed zone-boundary modes in our sample, we performed polarized Raman mapping on adjacent domains of $n = 2$ Br-RPP at 80 K. A new peak at ≈60 $cm^{-1}$ was observed below 270 K (Figure S4, Supporting Information), which is attributed to anharmonic octahedral tilting. This peak is not related to the ferroelectric phase transition which is beyond the scope of this work. Here, we focus on the Raman modes at ≈34 and ≈46 $cm^{-1}$, which remain Raman-active at room temperature. As shown in **Figure 5a,b**, the Raman modes at ≈34 and ≈46 $cm^{-1}$ exhibit similar periodic variations in the adjacent domains A and B of $n = 2$ Br-RPP. Notably, the phonon at ≈46 $cm^{-1}$ is identified as the characteristic ferroelectric phonon in $n = 2$ Br-RPP, while the phonon at ≈34 $cm^{-1}$ serves as a common phonon for comparison. Both ≈34 and ≈46 $cm^{-1}$ modes demonstrate a $\pi/2$ phase change with a biaxial character. However, it is noteworthy that the ≈46 $cm^{-1}$ phonon in $n = 2$ Br-RPP shows a directional dependence that correlates with the orientation of the polar axis in the separated domains A and B (Figure 5c,d). In contrast, no such directional dependence is observed for the ≈34 $cm^{-1}$ mode (Figure 5e,f). This is further confirmed by the orthogonality of the adjacent polar axes of ≈46 $cm^{-1}$ polar mode in the neighboring ferroelectric domains of $n = 2$ Br-RPP (Figure 5c,d). This observation explains why the ≈46 $cm^{-1}$ mode has been assigned as the characteristic ferroelectric mode in our previous discussion and provide additional evidence for the zone-boundary modes driving ferroelectric phase transition.

Based on this effect, we can utilize the ≈46 $cm^{-1}$ ferroelectric phonon to map the orientations of the ferroelectric domains. Figure 5g–i show the linearly polarized Raman maps for perpendicular ferroelectric domains architecture in $n = 2$ Br RPP films. The maps clearly show domains with orthogonal polarizations. When the linear polariser rotates from 45° to 135°, different sets of striped domains become bright or dark concurrently (Figure 5h,i), enabling us to identify domains with the same polarized orientation. We notice that the neighboring ferroelectric domains are perpendicular to each other, forming a 90°-domain wall between the $c$-axes and $b$-axes of two adjacent domains. In addition to perpendicular domains, we also performed polarized Raman mapping on parallel-geometry domain of $n = 2$ Br-RPP (Figure 5j). Figure 5k,l display the domain geometry and polarized Raman maps at ≈46 $cm^{-1}$ under incident laser angles of 45° and 135°, respectively. Intriguingly, despite the parallel alignment of the domains, the polarization axes of adjacent domains across the boundary exhibit a 90° orthogonal relationship. Such polarized Raman phenomenon is absent in the ≈34 $cm^{-1}$ phonon (Figures S5 and S6, Supporting Information). For $n = 3$ Br-RPP, the ferroelectric phonon at ≈33 $cm^{-1}$, previously identified as a fingerprint of the ferroelectric phase, similarly reveals orthogonal polarization axes between neighboring domains (Figure S7, Supporting Information). This observation aligns with the reduced energy barrier for polarization switching in $n = 3$ systems, as discussed earlier, and underscores the role of dimensionality in modulating domain-related phonon interactions.

## 3. Conclusions

We conducted systematic Raman spectroscopy studies on RPP-based ferroelectrics to identify phonon signatures linked to ferroelectricity. A reversible phonon was observed during the ferroelectric-paraelectric phase transition, serving as a fingerprint ferroelectric phonon. DFT calculations simulated the phase transition and identified zone-boundary phonons responsible for driving the transition, with simulated Raman spectra matching experimental observations. Notably, these ferroelectric phonons exhibit a redshift in higher-$n$ value HOIP ferroelectrics compared to their lower-$n$ counterparts. This $n$-dependent redshift correlates with a reduced energy barrier for ferroelectric switching in higher-$n$ HOIPs, consistent with their enhanced switching dynamics. Polarized Raman mapping using the ferroelectric phonon revealed adjacent ferroelectric domains with orthogonal polar axes, confirming the "twin" domain structure in Br-RPPs. The polarization directions across domain boundaries are mutually perpendicular, reflecting the symmetry-breaking nature of the ferroelectric transition. These results clarify the origin of ferroelectricity in HOIPs and establish Raman-active modes as probes for domain-specific ferroelectric properties, offering insights for applications in ferroelectric memory and polarization-sensitive optoelectronics.

## 4. Experimental Section

*Sample Preparation*: A series of single crystals, $(BA)_2(MA)_{n\text{-}1}Pb_nBr_{3n+1}$ ($n$ = 1–3), were synthesized using temperature-controlled cooling methods. The precursor molar ratios for the synthesis of $(BA)_2PbBr_4$, $(BA)_2(MA)Pb_2Br_7$, and $(BA)_2(MA)_2Pb_3Br_{10}$ were as follows: 0.59 M BABr (Greatcell Solar Ltd), 0 M MABr (Greatcell Solar

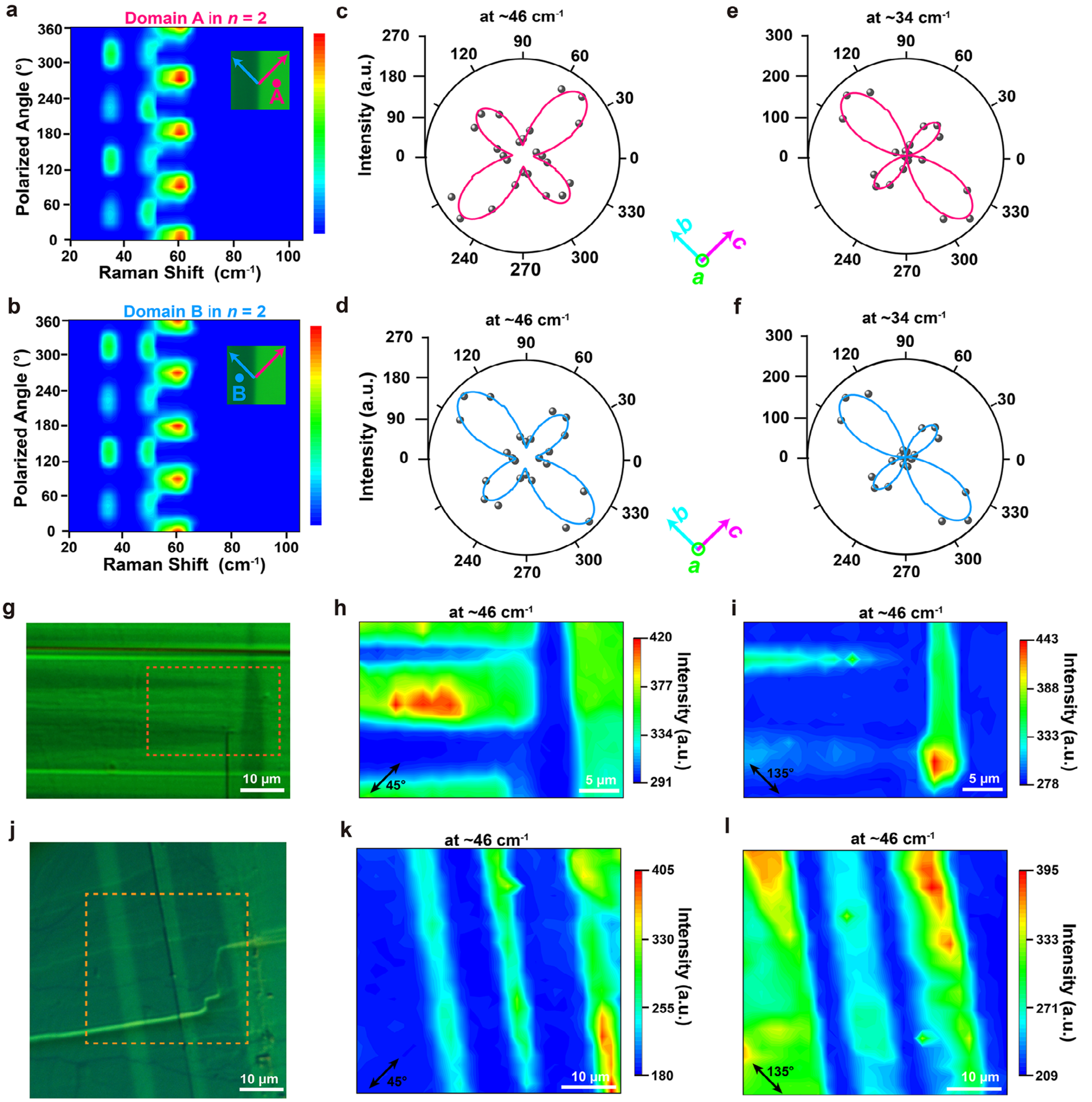

**Figure 5.** Polarized Raman spectrum and mapping of ferroelectric domains with different architectures in $n = 2$ Br-RPPs. a,b) Intensity maps of Raman spectra for the adjacent ferroelectric domains A and B in $n = 2$ Br-RPP at different polarized angles, with 0° aligned to the vertical direction of ferroelectric domain wall. c–f) Polar plots of Raman intensity at ≈46 and ≈34 cm$^{-1}$ for the adjacent ferroelectric domains A and B, respectively. g–i) POM image and corresponding polarized Raman mapping of the square dashed area in g) at ≈46 cm$^{-1}$, under incident laser polarization angle of 45° in h), and 135° in i). j–l) POM image of a different domain geometry and corresponding polarized Raman mapping of the square dashed area in j) at ≈46 cm$^{-1}$, under incident laser polarization angles at 45° in k) and 135° in l).

Ltd), and 0.40 M PbO (Sigma–Aldrich); 0.59 M BABr, 0.21 M MABr, and 0.40 M PbO; and 0.29 M BABr, 0.41 M MABr, and 0.40 M PbO, respectively. Each batch of these precursors was mixed with a solvent of HBr (0.9 mL, 48 wt.% in $H_2O$, Sigma–Aldrich) and $H_3PO_2$ (0.1 mL, 50 wt.% in $H_2O$, Sigma–Aldrich). The resulting solution was heated to 110 °C while being stirred vigorously for 1 h and then allowed to cool to room temperature at a rate of 1 °C per day. The crystals formed were collected from the solution and vacuum-dried overnight. Finally, it was mechanically exfoliated the single crystals onto a $SiO_2$/Si substrate for further analysis.

*DSC Measurement*: For the DSC measurements, the samples were placed in aluminum crucibles and maintained under a nitrogen atmosphere. The heating and cooling rates were set to 10 K min$^{-1}$ using a DSC3 instrument (Mettler-Toledo, Inc.).

*Temperature-Dependent Observation of Ferroelectric Domains and SHG Collection*: POM images were captured using a Leica CCD camera, with a polarizer positioned in front of the CCD to facilitate the observation of ferroelectric domains. The samples were mounted in a Linkam holder and maintained under a nitrogen atmosphere for temperature-dependent POM imaging. For the SHG measurements, a continuous-wave laser operating at 1064 nm (Rainbow 1064 OEM) was utilized. During these measurements, the samples were placed in the Linkam holder under vacuum conditions to ensure accurate temperature-dependent data collection.

*Ferroelectric P-E loop and PFM Measurement*: The ferroelectric *P-E* loop of single-crystal perovskites was measured using the Precision Premier II Ferroelectric Tester (Radiant Technologies), equipped with an external amplifier and high-voltage interface. To prevent degradation during measurements, the samples were maintained in an oil bath. PFM measurements were conducted using a commercial Bruker Dimension Icon microscope at Ar-filled glovebox. A conductive Pt/Ir-coated tip with a force constant of 2.8 N $m^{-1}$ was employed, along with an AC drive voltage ranging from 3.0 to 3.5 V, to visualize PFM and facilitate polarization switching in the ferroelectric domains.

*Raman Measurements*: Raman spectroscopy was conducted using a confocal WiTec Alpha 300R Raman microscope, which is equipped with a 633 nm laser. The laser was focused on an area of ≈1 $\mu m^2$ using a 50× objective (*NA* 0.5). To prevent laser-induced damage, the laser power on the sample was maintained at 2.0 mW. All samples were placed in a Linkam holder under vacuum conditions during the measurements. For temperature-dependent Raman spectroscopy, the sample was initially cooled to 80 K, after which the temperature was gradually increased to the desired values. For the polarization-dependent Raman spectroscopy measurements, as shown in Figure S8 (Supporting Information), it was used two linear polarizers and a half-wave ($\lambda/2$) plate: the first linear polarizer (P1) was placed in the incident beam path to adjust the initial polarization of the laser, with its angle fixed at 0°. The $\lambda/2$ plate was integrated into the incident light path to control the polarization of the laser. The backscattered light was collected and passed through the $\lambda/2$ plate, while the second linear polarizer (P2) was placed in the detection beam path with its angle also fixed at 0°. During the experiment, P1 and P2 were always maintained at the same polarization angle, ensuring a parallel orientation. The $\lambda/2$ plate was automatically rotated to adjust the polarization of the incident laser, allowing for the acquisition of the Raman spectra at different polarization angles. Spatial Raman mappings were performed under vacuum conditions at 80 K.

*DFT Calculations*: It was employed DFT to calculate the structure and phonon properties of $(BA)_2(MA)Pb_2Br_7$ and $(BA)_2(MA)_2Pb_3Br_{10}$ using the CASTEP software package.[42] The simulations utilized a plane-wave basis combined with norm-conserving pseudopotentials from the CASTEP standard library.[43] The exchange-correlation interaction was modeled using the Perdew-Burke-Ernzerhof generalized gradient approximation,[48] while van der Waals interactions between ions were accounted for using the Tkatchenko-Scheffler empirical dispersion correction. During geometry optimization, the energy cutoff was set to 1200 eV, and a 1×2×2 Monkhorst-Pack *k*-point grid was employed.[49] The structure was fully relaxed until the forces between atoms fell below 0.005 eV $Å^{-1}$. For the phonon calculations, the force matrix was determined using density-functional perturbation theory. Subsequently, the modes at the $\Gamma$-point and the corresponding Raman spectrum for the LS phase was investigated. After the projection of these modes onto the HS phase, the *ISODISTORT* tool to decompose the modes into intrinsic symmetry-adapted modes of the HS phase for the symmetry mode analysis was used.[44] Polarization calculations were performed on the basis of the Berry phase theory.[46] In the point-charge model calculations, the Bader analysis to determine the charge on each ion was adapted.[47]

## Supporting Information

Supporting Information is available from the Wiley Online Library or from the author.

## Acknowledgements

C.L. and S.Y. contributed equally to this work. K.L. acknowledges the fundings from the Croucher Foundation (Croucher Tak Wah Mak Innovation fund 2023) and Project 62322413 supported by National Natural Science Foundation of China and the Research Grants Council of the Hong Kong Special Administrative Region, China (Project No. PolyU25305222, PolyU15304623, and PolyU15306724). K. P. L. acknowledges Hong Kong's JC STEM Lab of 2D Quantum Materials project P0043063.

## Conflict of Interest

The authors declare no conflict of interest.

## Data Availability Statement

The data that support the findings of this study are available from the corresponding author upon reasonable request.

## Keywords

2D hybrid perovskite ferroelectric, domains, ferroelectric switching, phase transition, polarized Raman spectroscopy

Received: December 15, 2024
Revised: May 23, 2025

[1] K. Leng, R. Li, S. P. Lau, K. P. Loh, *Trends Chem* **2021**, *3*, 716.
[2] D. Meier, S. M. Selbach, *Nat. Rev. Mater.* **2021**, *7*, 157.
[3] S. D. Stranks, P. Plochocka, *Nat. Mater.* **2018**, *17*, 381.
[4] H. Kikuchi, H. Nishikawa, H. Matsukizono, S. Iino, T. Sugiyama, T. Ishioka, Y. Okumura, *Adv. Sci.* **2024**, *11*, 2409827.
[5] A. K. Kalyani, R. Garg, R. Ranjan, *Appl. Phys. Lett.* **2009**, *94*, 202903.
[6] R. E. Cohen, *Nature* **1992**, *358*, 136.
[7] T. Qi, I. Grinberg, A. M. Rappe, *Phys. Rev. B* **2010**, *82*, 134113.
[8] L. Kuerten, S. Krohns, P. Schoenherr, K. Holeczek, E. Pomjakushina, T. Lottermoser, M. Trassin, D. Meier, M. Fiebig, *Phys. Rev. B* **2020**, *102*, 094108.
[9] P. Meisenheimer, X. Huang, G. Moore, S. Zhou, S. Husain, X. Chen, H. Zhang, L. W. Martin, K. A. Persson, S. Griffin, L. Caretta, P. Stevenson, R. Ramesh, *Nat. Commun.* **2024**, *15*, 2903.
[10] N. A. Benedek, C. J. Fennie, *Phys. Rev. Lett.* **2011**, *106*, 107204.
[11] C. Li, M. Telychko, Y. Zheng, S. Yuan, Z. Wu, W. P. D. Wong, Y. Li, Y. Jin, W. F. Io, X. Wang, J. Lin, J. Hao, C. Han, K. Leng, *Nat. Commun.* **2024**, *15*, 10221.
[12] Z.-G. Li, M. Zacharias, Y. Zhang, F. Wei, Y. Qin, Y.-Q. Yang, L.-C. An, F.-F. Gao, W. Li, J. Even, X.-H. Bu, *ACS Energy Lett.* **2023**, *8*, 3016.
[13] M. Menahem, Z. Dai, S. Aharon, R. Sharma, M. Asher, Y. Diskin-Posner, R. Korobko, A. M. Rappe, O. Yaffe, *ACS Nano* **2021**, *15*, 10153.
[14] H.-Y. Zhang, Z.-X. Zhang, X.-J. Song, X.-G. Chen, R.-G. Xiong, *J. Am. Chem. Soc.* **2020**, *142*, 20208.
[15] W. He, Y. Yang, C. Li, W. P. D. Wong, F. Cimpoesu, A. M. Toader, Z. Wu, X. Wu, Z. Lin, Q. Xu, K. Leng, A. Stroppa, K. P. Loh, *J. Am. Chem. Soc.* **2023**, *145*, 14044.
[16] Z. Wu, W. Zhang, H. Ye, Y. Yao, X. Liu, L. Li, C. Ji, J. Luo, *J. Am. Chem. Soc.* **2021**, *143*, 7593.
[17] A. Baldwin, G. Delport, K. Leng, R. Chahbazian, K. Galkowski, K. P. Loh, S. D. Stranks, *J. Phys. Chem. Lett.* **2021**, *12*, 4003.
[18] J. Y. Park, R. Song, J. Liang, L. Jin, K. Wang, S. Li, E. Shi, Y. Gao, M. Zeller, S. J. Teat, P. Guo, L. Huang, Y. S. Zhao, V. Blum, L. Dou, *Nat. Chem.* **2023**, *15*, 1745.

[19] B. Dhanabalan, Y.-C. Leng, G. Biffi, M.-L. Lin, P.-H. Tan, I. Infante, L. Manna, M. P. Arciniegas, R. Krahne, *ACS Nano* **2020**, *14*, 4689.
[20] C. Li, K. P. Loh, K. Leng, *Matter* **2022**, *5*, 4153.
[21] B. L. Wooten, R. Iguchi, P. Tang, J. S. Kang, K.-I. Uchida, G. E. W. Bauer, J. P. Heremans, *Sci. Adv.* **2023**, *9*, 7194.
[22] G. Yumoto, F. Harata, T. Nakamura, A. Wakamiya, Y. Kanemitsu, *Sci. Adv.* **2024**, *10*, 5521.
[23] S. Song, H. M. Jang, N.-S. Lee, J. Y. Son, R. Gupta, A. Garg, J. Ratanapreechachai, J. F. Scott, *NPG Asia Mater* **2016**, *8*, 242.
[24] H. M. Jang, M.-A. Oak, J.-H. Lee, Y. K. Jeong, J. F. Scott, *Phys. Rev. B* **2009**, *80*, 132105.
[25] Y. Chen, Y. Lei, Y. Li, Y. Yu, J. Cai, M.-H. Chiu, R. Rao, Y. Gu, C. Wang, W. Choi, H. Hu, C. Wang, Y. Li, J. Song, J. Zhang, B. Qi, M. Lin, Z. Zhang, A. E. Islam, B. Maruyama, S. Dayeh, L.-J. Li, K. Yang, Y.-H. Lo, S. Xu, *Nature* **2020**, *577*, 209.
[26] M. Mączka, M. Ptak, *J. Phys. Chem. C* **2022**, *126*, 7991.
[27] T. Yin, H. Yan, I. Abdelwahab, Y. Lekina, X. Lü, W. Yang, H. Sun, K. Leng, Y. Cai, Z. X. Shen, K. P. Loh, *Nat. Commun.* **2023**, *14*, 411.
[28] D. Bansal, J. L. Niedziela, R. Sinclair, V. O. Garlea, D. L. Abernathy, S. Chi, Y. Ren, H. Zhou, O. Delaire, *Nat. Commun.* **2018**, *9*, 15.
[29] S. Li, T. Birol, *npj Comput. Mater.* **2020**, *6*, 168.
[30] J. Gu, Y. Tao, T. Fu, S. Guo, X. Jiang, Y. Guan, X. Li, C. Li, X. Lu, Y. Fu, *Angew. Chem., Int. Ed.* **2023**, *62*, 202304515.
[31] X. Huang, X. Li, Y. Tao, S. Guo, J. Gu, H. Hong, Y. Yao, Y. Guan, Y. Gao, C. Li, X. Lü, Y. Fu, *J. Am. Chem. Soc.* **2022**, *144*, 12247.
[32] C. Gehrmann, D. A. Egger, *Nat. Commun.* **2019**, *10*, 3141.
[33] Z. Wu, S. Li, Y. M. Yousry, W. P. D. Wong, X. Wang, T. Ma, Z. Chen, Y. Shao, W. H. Liew, K. Yao, F. Pan, K. P. Loh, *Nat. Commun.* **2022**, *13*, 3104.
[34] W. S. Huxter, M. F. Sarott, M. Trassin, C. L. Degen, *Nat. Phys.* **2023**, *19*, 644.
[35] Y. Qin, Z. G. Li, F. F. Gao, H. Chen, X. Li, B. Xu, Q. Li, X. Jiang, W. Li, X. Wu, Z. Quan, L. Ye, Y. Zhang, Z. Lin, L. Pedesseau, J. Even, P. Lu, X. H. Bu, *Adv. Mater.* **2022**, *34*, 2201666.
[36] L. Li, X. Liu, Y. Li, Z. Xu, Z. Wu, S. Han, K. Tao, M. Hong, J. Luo, Z. Sun, *J. Am. Chem. Soc.* **2019**, *141*, 2623.
[37] X. Xiao, J. Zhou, K. Song, J. Zhao, Y. Zhou, P. N. Rudd, Y. Han, J. Li, J. Huang, *Nat. Commun.* **2021**, *12*, 1332.
[38] E. Shi, S. Deng, B. Yuan, Y. Gao, L. Y. Akriti, C. S. Davis, D. Zemlyanov, Y. Yu, L. Huang, L. Dou, *ACS Nano* **2019**, *13*, 1635.
[39] M. Zacharias, G. Volonakis, F. Giustino, J. Even, *npj Comput. Mater.* **2023**, *9*, 153.
[40] A. Cohen, T. M. Brenner, J. Klarbring, R. Sharma, D. H. Fabini, R. Korobko, P. K. Nayak, O. Hellman, O. Yaffe, *Adv. Mater.* **2022**, *34*, 2107932.
[41] N. S. Dahod, A. France-Lanord, W. Paritmongkol, J. C. Grossman, W. A. Tisdale, *J. Chem. Phys.* **2020**, *153*, 044710.
[42] S. J. Clark, M. D. Segall, C. J. Pickard, P. J. Hasnip, M. J. Probert, K. Refson, M. C. Payne, *Z. Kristallogr.* **2005**, *220*, 567.
[43] M. C. Payne, M. P. Teter, D. C. Allan, T. A. Arias, J. D. Joannopoulos, *Rev. Mod. Phys.* **1992**, *64*, 1045.
[44] H. T. Stokes, D. M. Hatch, B. J. Campbell, D. E. Tanner, *J. Appl. Crystallogr.* **2006**, *39*, 607.
[45] Q.-Q. Jia, L. Tong, M.-M. Lun, D.-W. Fu, T. Zhang, H.-F. Lu, *Cryst. Growth Des.* **2022**, *22*, 2799.
[46] N. A. Spaldin, *J. Solid State Chem.* **2012**, *195*, 2.
[47] W. Tang, E. Sanville, G. Henkelman, *J. Phys.: Condens. Matter* **2009**, *21*, 084204.
[48] J. P. Perdew, A. Ruzsinszky, G. I. Csonka, O. A. Vydrov, G. E. Scuseria, L. A. Constantin, X. Zhou, K. Burke, *Phys. Rev. Lett.* **2008**, *100*, 136406.
[49] A. Tkatchenko, M. Scheffler, *Phys. Rev. Lett.* **2009**, *102*, 073005.